Use of magnesium-silicate-hydrate (M-S-H) cement mixes in 3D printing applications

Biranchi Panda[1,3], Cem Sonat[2], En-Hua Yang[2], Ming Jen Tan[1], Cise Unluer[4,*]

[1] Singapore Centre for 3D Printing, School of Mechanical & Aerospace Engineering, Nanyang Technological University, 50 Nanyang Avenue, Singapore 639798

[2] School of Civil and Environmental Engineering, Nanyang Technological University, 50 Nanyang Avenue, Singapore 639798

[3] Department of Mechanical Engineering, Indian Institute of Technology Guwahati, India

[4] School of Engineering, University of Glasgow, Glasgow G12 8LT, United Kingdom

* Corresponding author. E-mail address: Cise.Unluer@glasgow.ac.uk

Abstract

This study focused on the development of 3D printed building components incorporating MgO-SiO_2 binders. The effects of parameters such as MgO/SiO_2 and water/binder ratios and superplasticizer dosage were evaluated to produce 3D printable MgO-SiO_2 binders. The assessment of rheological and mechanical properties, which led to an optimum mix that satisfied the printability criteria, was supported by microstructural characterization. The best-performing mix in terms of printability and mechanical performance was characterized via x-ray diffraction (XRD), thermogravimetric analysis/derivative thermogravimetry (TG/DTG) and field emission scanning electron microscopy (FESEM) with energy dispersive spectroscopy (EDS). The selected mix exhibited thixotropic behaviour with an ability to recover ~80% of its original viscosity within 60 seconds of extrusion and a shape retention factor of ~1. The extrudability, shape retention and buildability aspects were successfully demonstrated by printing a 5-layered 3D structure without any deformations. The final product contained brucite and M-S-H as hydration products, which were the main contributor to mechanical performance and microstructural densification.

Keywords: 3D concrete printing; MgO; M-S-H; thixotropy; performance; microstructure

1. Introduction

Additive and automated manufacturing technologies involving cementitious materials such as 3D concrete printing have experienced continuous worldwide development over the past years. Digital concrete has rapidly evolved from an idea to a feasible alternative to conventional technologies with expanding application areas [1, 2]. The use of 3D printing can shorten the construction process, enhance resource efficiency, reduce construction waste, enable worker distancing (i.e. especially important in global pandemics such as COVID-19), and facilitate complex, high-quality and functional designs that would either be not feasible or too costly with conventional building methods. One of the aspects that needs to be considered for 3D-printed concrete mixes involves the development of binders with adequate rheological and stiffening properties to enable their continuous pumping during the initial stages, followed by shape retention after extrusion [3, 4].

Along with extrudability (i.e. pumpability), another property that is considered in the mix design of 3D printing is buildability. Pumpability refers to the effort needed for transferring the material from the mixer/reservoir to the nozzle; whereas buildability is dependent on the material yield stress and structural build-up properties [5-8]. These aspects can be assessed by measuring the yield stress and viscosity of the material. For a given layer to be stable after extrusion, an adequate yield stress must be reached after deposition, which can be controlled by the flocculation process [9]. Flocculation refers to the formation of clusters by the growth of cement particles in dispersion, contributing to the development of yield strength in the material. Accordingly, in order to achieve a stable filament, the printed material must show the ability to flocculate immediately after its deposition. In the case of the multi-layer deposition processes, gravity-induced stresses progressively increase with an increase in the number of layers. During this process, the rate of structural build-up needs to be controlled by the use of suitable admixtures, without sacrificing the inter-layer bond strength. These properties can be achieved via the optimisation of the mix design, resulting in a balance between continuous flowability during extrusion and proper structuration after deposition, thereby enabling the production of a robust 3D printed component [10].

Previous studies [11-15] have reported the key factors controlling the fresh properties (e.g. rheology) of 3D printable cement-based mixes. However, most of the mixtures designed for 3D

printing involve the use of Portland cement (PC) as the main binder component. The production of PC accounts for 5-7% of the global anthropogenic carbon dioxide (CO_2) emissions. In this regard, reactive magnesium oxide (MgO)-based cements present some advantages over PC such as the lower calcination temperatures used during their production in comparison to PC (700°C vs. 1450°C) and their ability to be extracted from waste sources (i.e. reject brine). The combination of MgO with a silica (SiO_2) source leads to the formation of magnesium silicate hydrate (M-S-H), which provides strength within concrete formulations, without requiring any special curing arrangements such as accelerated CO_2 curing [16, 17]. The characteristics of M-S-H are controlled by several factors including the type and properties of binder components, mix design (i.e. initial MgO/SiO_2 ratio, water-to-binder ratio and superplasticizer content) and curing conditions [18, 19]. Previous studies have looked into the effect of different raw materials [20, 21], role of superplasticizers [22, 23], durability and mechanical properties [17, 24] and microstructural characterization [25, 26] of the final products in the MgO-SiO_2 binders. With high initial compressive strengths reaching up to 70 MPa after 28 days of curing [27], MgO-SiO_2 binders have the potential to be used as structural or non-structural building components. These initially high strengths enable a higher shape retention and lower filament deformation during 3D printing. Additionally, due to their intrinsically low pH (~10.5) in comparison to PC (~12.5), MgO-SiO_2 binders can be utilized in applications involving natural fibre reinforcements [28, 29] and waste encapsulation [30, 31], which can widen the application spectrum of 3D printed components.

In line with the global academic and industrial initiatives on enhancing the sustainability of cement-based mixes, this paper focused on the development of 3D printed building components incorporating alternative binders such as MgO-SiO_2 binders with potentially lower environmental impacts. The use of MgO-SiO_2 binders in 3D printing, which has not been studied until now, was aimed to pave the way for the development of alternative binder systems for 3D printing applications and provide new insights on the printability aspects of these mixes. This was achieved via the examination of the key factors controlling the design of 3D printable MgO-SiO_2 binders such as the rheological properties of materials in the fresh state and printed region based on thixotropy, slump and flow diameter values. The effects of parameters such as MgO/SiO_2 and water-to-binder (w/b) ratios and superplasticizer (SP) dosage were assessed in order to produce sustainable 3D printable mixtures. Out of the formulations investigated in this study, the mix that

exhibited the best printability and mechanical performance was further characterized in terms of its composition (i.e. phase formations) and microstructural development via x-ray diffraction (XRD), thermogravimetric analysis/derivative thermogravimetry (TG/DTG) and field emission scanning electron microscopy (FESEM) with energy dispersive spectroscopy (EDS).

2. Materials and Methodology

2.1 Materials and mix preparation

Reactive MgO (labelled as "calcined magnesite 92/200") was provided by Richard Baker Harrison (UK), whereas microsilica (MS) (labelled as "940U") was provided by Elkem Materials (Singapore). The chemical compositions and physical properties of these binder components are shown in Table 1. The superplasticizer (SP) used in the prepared formulations was sodium hexametaphosphate (SHMP), provided by VWR (Singapore).

Table 2 shows all the different mix compositions used in this study. Two different binder compositions were prepared, in which the MgO:MS proportions were set at 50:50 and 70:30. For each composition, two different water-to-binder (w/b) ratios (0.4 and 0.5) and SP dosages (1.5 wt.% and 2.5 wt.% of the binder) were used, generating eight mix designs in total. These levels were determined based on the preliminary extrudability test results and minimum M30 grade concrete (compressive) strength requirement. Mix preparation initiated by dissolving SHMP in water to form a superplasticizer solution. After the SHMP was fully dissolved in water, MgO was added into the SHMP solution while mixing in a Hobart HL200 mixer. MS was then gradually added to the mix and the mixing continued for 5 minutes, until a thoroughly mixed paste was obtained.

2.2 Methodology

2.2.1 Slump and flow table

The slump value of cement-based mixes is related to their static yield stress, whereas the flow diameter is related to viscosity [32]. Accordingly, to assess these fresh properties, a conical mould, as shown in Fig. 1(a), was used for the slump and flow table tests, in accordance with ASTM C230 [33]. The test procedure started by filling the prepared pastes into the mould, after which the excess material was taken out and the surface was smoothened with a trowel. This was followed by the removal of the mould, after which the change in height was measured and reported as the slump value. The flow table test setup is demonstrated in Fig. 1(b), which was performed in accordance with ASTM C1437 [34]. To measure the flow values, the flow table was dropped 25 times after the mould was removed and the diameter of the paste was recorded.

2.2.2 Thixotropy (viscosity recovery)

Thixotropy, assessed by the viscosity recovery test, is a desirable aspect for 3D printing, referring to the state of high viscosity at low stress and vice versa. A constant shear rate of 300 s^{-1} was applied for the evaluation of the shear thinning property, while viscosity recovery was assessed via a three-stage approach, whose details were provided in [35]. The thixotropy of the prepared mixes was measured by a MCR 101 model rheometer from Anton Paar. The approach adopted in determining the shear rates and timings used during this 3-step analysis aimed to simulate the printing process, during which the prepared mix is initially at rest in the hopper, then experiences high shear during extrusion, followed by its resting on the print bed.

2.2.3 3D printing

The success of the printing process was evaluated according to two main aspects: (i) the effort needed to extrude the material through the printer nozzle, thereby assessing its extrudability and (ii) the stability of the layers forming the component, indicating its buildability. Accordingly, a 4-axis gantry printer, whose details were provided in [36], was employed in the printing of the designed mixes via the use of a nozzle that had a width of 30 mm and a layer height of 15 mm.

The printer was connected to a screw pump. The optimum speed for the mixes was determined by varying the print speed from 60 to 100 mm/sec, while the flow rate was kept constant, with the goal of maintaining the shape stability of the filaments. The shape retention factor (SRF) for selected mixes was obtained by dividing the width of the printed filament with the width of the rectangular nozzle (30 mm). A digital imaging technique was used to capture the width of the filament after the deposition of each layer. The obtained photos were analysed with "ImageJ", an image processing program to accurately determine the width of the printed filament. Finally, a freeform design was printed by using the best flow rate and speed combination to validate the feasibility of using the proposed criteria and mix design in practice.

2.2.4 Green strength

Uniaxial unconfined compression tests were performed on freshly prepared cylindrical samples with a diameter of 70 mm and a height of 140 mm, as shown in Fig. 2. These samples were kept in moulds for 15 minutes (i.e. replicating the approximate time interval from mixing to printing, to reveal the mix condition during the printing process) before the mould was carefully removed to expose the sample without any damage. The dimensions were chosen to avoid any variations on the results due associated with particle size, leading to a diagonal shear failure [37]. An INSTRON 5969 test rig equipped with a 50 kN load cell was used at a loading rate of 0.6 N/s for strength testing, which was selected to simulate the loading steps in the printing process. Each test was conducted at ~60 to 70 seconds to avoid the influence of thixotropic build-up. The averages of the obtained values were presented in the load and deformation diagram.

2.2.5 Compressive strength

Samples were cast into 50×50×50 mm cubic moulds and their average 28-day compressive strength values were reported in Table 4. For the 3D printed samples, blocks with the dimensions of 300×150×200 mm were printed by using a 20 mm circular nozzle at a print speed of 90 mm/sec and flow rate of 3.15 g/lit. A circular nozzle was preferred as the blocks were printed without any

nozzle rotation. 50×50×50 mm cubes were then extracted from these blocks by using a saw. The compressive strengths of 50×50×50 mm cubic samples after 28 days of ambient curing (temperature of 30±2°C and relative humidity (RH) of 60±5%) were measured by three directional uniaxial loading, in line with ASTM C109/C109-M13 [38]. The test was performed via the use of a Toni Technik Baustoffprüfsysteme machine, during which the loading rate was set at 55 kN/min. Each data point represented the average of four samples, accompanied with their standard deviation.

2.2.6 Characterization of reaction products (XRD, TG/DTG, FESEM-EDS)

The compositions and morphologies of the phases that formed were evaluated via microstructural tests in order to shed light on the mechanism behind the strength development of the 3D printed MgO-SiO_2 samples. To facilitate these investigations, segments carefully extracted from the 3D printed samples were kept in acetone for 3 days to stop hydration and vacuum dried before being ground down to pass through a 75 μm sieve in preparation for microstructural analyses.

The different phases within the hydrated samples were identified and characterized via x-ray diffraction (XRD) and thermogravimetry/derivative thermogravimetry (TG/DTG) analyses. XRD was performed on the ground powder extracted from the best performing samples after 28 days of curing, by using a Bruker D8 ADVANCE instrument with a scanning rate of 0.02° 2θ/step from 10° to 80° 2θ to identify the formed hydration products (e.g. M-S-H and brucite) as well as any unreacted phases. TG/DTG was carried out by a Perkin Elmer TGA 4000 equipment, which was operated under a constant nitrogen flow. Samples were heated from 30°C to 900°C at a heating rate of 10 °C/min. The morphology of the formed phases was observed via a JEOL JSM-7600F field emission scanning electron microscope (FESEM), at an accelerating voltage of 5.0 kV. In preparation for FESEM, the specimens were coated with platinum under 20 mA current for 30 seconds. Energy dispersive spectroscopy (EDS) measurements were used to determine the elemental composition of the 3D printed specimens at 28 days. The accelerating voltage used during this analysis was 15.0 kV.

3. Results and Discussion

3.1 Effect of mix design on slump, flow diameter and viscosity recovery

The results of slump and flow table tests of the prepared mixes were plotted in Fig. 3. As mix M1 led to a very dry and stiff mix because of a combination of low w/b ratio (0.4) and SP dosage (1.5%) in the presence of 50% MS, it was not shown in Fig. 3 and did not qualify for the subsequent pumpability test due to discontinuous filament extrusion. Amongst the remaining mixes, M3 and M5 revealed low values of slump and flow diameter, which was associated with their low w/b ratios (0.4) and/or SP dosage (1.5%). On the other hand, mixes M2, M4, M6 and M8, all of which had high w/b ratios (0.5), resulted in similar or high slump and flow diameter values; whereas mix M7 led to intermediate outcomes due to its low w/b ratio (0.4) but high SP dosage (2.5%). The higher water content within these mixes (i.e. M2, M4, M6, M8) reduced the interaction and internal friction amongst the particles, thereby resulting in a higher flowability. However, previous research [39] indicated that mixes with high slump values could experience elastic collapse during 3D printing, which would negatively affect the mechanical properties of the printed specimens by inducing porosity. Even though mixes M2 and M4 had similar slump values with mixes M5 and M7, their flow diameter values were significantly higher, which could result in challenges in retaining the printed shape and hinder the success of the overall 3D printing process. Therefore, mixes M3, M5 and M7 were chosen for further rheological assessment as a part of the evaluation of the suitability of these mixes for 3D printing.

Fig. 4 shows the shear recovery of the three mixes M3, M5 and M7 selected for the further investigation of their rheological properties. The results of viscosity recovery test were divided in three parts to mimic the 3D printing process, starting with (i) material at rest, (ii) material sheared or extruded at a high shear rate and (iii) material at rest again on the print bed. During this analysis, the viscosities before and after the extrusion process are important for the success of extrusion-based 3D printing. Accordingly, an ideal material should recover to its initial viscosity as soon as it is deposited on the print bed. The results shown in Fig. 4 revealed the ability of all three mixes to recover up to 80% of their original viscosities within 60 seconds of extrusion. Out of these

mixes, M3 exhibited slightly higher apparent viscosity values than the other two mixes with a reasonable recovery ability. This outcome could be an indication of the dense microstructure of M3, which was also shown by its low slump value and flow diameter in Fig. 3.

3.2 3D printability and mechanical performance

In this section, the printability of the three selected mixes was studied by using a 4-axis gantry printer. Table 3 shows the SRF values of these mixes that were extruded through a rectangular nozzle, indicating their shape stability. Amongst the three mixes, M3 revealed the lowest SRF value of ~1.0, followed by M5 (~1.84) and M7 (~2.32). The trend observed in the SRF values was in agreement with the rheological properties (i.e. slump and flow diameter values), in which M3 demonstrated the lowest slump/flow diameter, followed by M5 and M7. The combination of these outcomes could explain the enhanced viscosity recovery of mix M3, which also exhibited the best shape stability, as indicated by its SRF of ~1.0. However, these differences amongst the three samples do not necessarily translate into poor shape stability for the other two mixes (M5 and M7) as SRF is highly influenced by printing parameters such as print speed, flow rate and nozzle height. Considering the higher slump and flowabilities of mixes M5 and M7 than those of mix M3, they may require a higher print speed (> 90 mm/sec) to obtain a stable filament shape.

The 28-day compressive strengths of the selected samples are shown in Table 4. Out of the three mixes, mix M3 exhibited the highest 28-day compressive strength (44.3 MPa), which could be attributed to its denser microstructure, potentially linked with the higher degree of M-S-H formation (i.e. the composition of hydrate phases within mix M3 is shown in Section 3.4) [40]. The differences in the binder composition of mix M3 (MgO:MS of 50:50) when compared to mixes M5 and M7 (MgO:MS of 70:30) could explain the increased formation of M-S-H in mix M3 as opposed to the predominant formation of brucite in the presence of 70% MgO in mixes M5 and M7 [26, 41]. This was in line with the findings of previous studies [42], where the direct correlation between the strength development of MgO-SiO_2 samples cured under different conditions and M-S-H formation was identified.

Considering its ideal thixotropic properties demonstrated by its viscosity recovery, lowest SRF and highest compressive strength amongst the formulations investigated under this study, mix M3 was chosen for further analysis, during which it was used in the printing of a 3D component. The settings of the gantry printer were fixed at a print speed of 90 mm/sec and a flow rate of 3.15 g/lit, in line with the findings of previous studies [32]. The layer-by-layer extruded structure led to the building of the 3D component shown in Fig. 5. The printed component, whose dimensions were 300 mm (L) x 150 mm (W) x 100 mm (H), indicated a good shape retention as well as buildability properties, highlighting the suitability of mix M3 to be used in 3D printing applications without any discontinuity and deformation.

3.3 Green strength and directional mechanical properties

The buildability of mix M3 was highly related to its initial (green) strength. To indicate this relationship and provide a comparison to conventional mixes, the performance of mix M3 was compared with a PC-based mix, which was prepared with the same w/b ratio and without any other additives. The load-deformation curves of these two mixes, shown in Fig. 6, revealed the higher load carrying capacity of mix M3 than PC, which could be attributed to the differences in the reaction products and the binding network they formed within each mix [43]. However, the performance of the PC mix could be improved by reducing the w/b ratio [44], possibly resulting in similar outcomes as mix M3.

Another inherent property that must be considered in the evaluation of a potential mix for 3D printing is directional mechanical strength, which is associated with the layer-wise approach of the printing process. Fig. 7(a) demonstrates the main orthogonal directions F1, F2 and F3; whereas the 28-day compressive strengths of 3D printed samples prepared by using mix M3 in F1, F2 and F3 directions are presented in Fig. 7(b). While the analysed samples revealed comparable strengths in F2 and F3 directions, the highest strength was achieved in F1 direction. Similar anisotropic behaviour in terms of mechanical properties was also observed in other alternative binder systems (e.g. glass fibre reinforced geopolymer samples) [45]. However, due to the identical orientations of F1 and F3, it was hard to attribute this outcome to different layer directions. These strength

variations could also be due to the motion patterns of the material during the printing process, resulting in alterations in the sample microstructure [46]. Regardless of these slight variations observed in different directions, the strength results recorded at 28 days were generally comparable in all directions and with the strength of the directly cast samples, which highlighted the robustness of these 3D printed samples for various uses including load bearing applications.

3.4 Microstructural analyses (XRD, TG/DTG and FESEM-EDS)

The crystalline and amorphous phases present in the 3D printed M3 mix at 28 days were identified by using XRD analysis, as shown in Fig. 8. The main hydration products identified in this system were M-S-H gel, as indicated by the amorphous humps at ~26°, 35° and 60° 2θ [27]; and brucite ($Mg(OH)_2$), with the main crystalline peaks at 18.6° and 38.0° 2θ. Other than the formed hydration products, the presence of unreacted raw materials was notable. Accordingly, unreacted MgO (periclase) revealed its main peaks at ~42.9° and 62.3° 2θ with high intensities, while unreacted SiO_2 had an amorphous hump centred at ~23° 2θ. The presence of significant amount of unreacted MgO indicated that potentially higher strengths could have been achieved if a higher degree of hydration was realized. In addition to the mentioned phases, magnesium carbonate ($MgCO_3$), which was present as an impurity in MgO, was observed at 32.6° and 53.9° 2θ.

TG and DTG plots of the 3D printed M3 mix at 28 days are presented in Fig. 9(a) and (b), respectively. As can be seen in Fig. 9(a), almost 20% loss in mass was observed, which took place in multiple stages, when the sample was subjected to high temperatures of up to 900°C. The DTG curves (Fig. 9(b)) revealed detailed information about the decomposed phases. Accordingly, the first decomposition was completed at ~200°C, which could be attributed to the dehydration of the interlayer water of M-S-H [47, 48]. The following decomposition curve centred at ~400°C was due to brucite dehydroxylation [26, 27]. The curve that partially overlapped with brucite dehydroxylation was associated with M-S-H dehydroxylation, which also continued at higher temperatures [20, 26], as can be seen in Fig. 9(b). The final decomposition step of the M-S-H gel took place at ~750°C due to the dehydroxylation of the silanol groups [26, 48]. In addition to these hydrate phases, the decomposition of magnesite ($MgCO_3$), which was present as an impurity

within MgO used as a binder, occurred at ~650°C, revealing a minor curve in the DTG plot of the analysed sample. The decomposition patterns shown by the TG/DTG plots were in line with the XRD results, indicating the presence of M-S-H and brucite as the main hydrate phases, accompanied by undecomposed binder phases.

Fig. 10 shows the FESEM image of the 3D printed M3 mix at 28 days. In line with the XRD and TG/DTG results, a majority of the sample microstructure was comprised of a widespread formation of M-S-H gel, which was the main contributor of strength in MgO-SiO_2 samples [49]. Along with M-S-H, spherical particles indicative of unreacted SiO_2 were observed. Furthermore, plate-like hydrates smaller than 1 μm, which resembled brucite crystals [50], could be seen in multiple locations within the microstructure. Overall, the continuous gel-like structure established by M-S-H covered the particle surfaces, leading to the formation of a dense microstructure, which contributed to mechanical performance, enabling the potential use of mix M3 in various building applications.

EDS analysis was also performed on mix M3 after 28 days by using the 14 arbitrarily chosen areas within the region shown in Fig. 11(a). A representative elemental analysis of one of the areas indicated by the rectangular box (i.e. Spectrum 8) in Fig.11(a) was presented in Fig. 11(b). The average and standard deviations of the values obtained from the measurements taken from 14 different areas were listed in Table 5. The elements O, Mg and Si were dominantly present within the measurement territory, highlighting the formation of M-S-H as well as brucite (i.e. composed of only Mg and O). The weight percentages of O, Mg and Si were around 52%, 21% and 21%, respectively. On top of these 3 elements, presence of ~6 wt.% carbon (C) was observed, which could be attributed to magnesite that was present as an impurity within MgO and the partial absorption of CO_2 from the atmosphere during sample preparation and curing.

4. Conclusions

This paper focused on the development of MgO-SiO_2 binders to be used in 3D printing applications. The effects of parameters such as water-to-binder (w/b) ratio, MgO/SiO_2 ratio and

superplasticizer (SP) dosage were assessed in order to produce sustainable 3D printable MgO-SiO_2 binders. The assessment of fresh properties was supported with mechanical testing and microstructural characterization. The following conclusions can be drawn from this study:

- The thixotropic behaviour of the developed mixes, which recovered 70-80% of their original viscosity within 60 seconds of extrusion, enabled the deposition of printed layers in 60 second intervals, without any pumpability issues.
- Out of the different formulations prepared in this study, the best-performing mix that satisfied the performance (i.e. high strength) and printability criteria (i.e. low slump and high flow) was determined.
- The selected mix (M3) indicated a SRF of ~1, highlighting its buildability potential, which was successfully demonstrated via the 3D printing of a 5-layered structure without any deformations.
- The anisotropic mechanical performance displayed by the printed samples, in comparison to the cast specimens, could be associated with the layer-wise fabrication approach adopted in the printing process. In spite of these differences, satisfactory strengths were obtained in all 3 directions.
- Microstructural characterization revealed the formation of brucite and M-S-H gel as the main hydration products, which were the main contributor to the mechanical performance observed within the prepared samples.

The findings of this research paved the way for the development of alternative MgO-SiO_2 binders for 3D printing applications and presented new insights on the printability aspects of these mixtures under the context of 3D printing, which have not been studied until now. Overall, the results of this study have shown that MgO-SiO_2 binders with proper mix designs are suitable to be used in 3D printing applications, both in terms of their rheological and mechanical properties. Considering the need for the optimization of these formulations for enhanced performance as well as an improved understanding of the mechanisms behind strength and microstructural development, further studies will focus on the enhancement of the performance of MgO-SiO_2 binders through an optimization of their fresh and long-term properties, with the overall goal of enabling their use in various building applications, including those involving 3D printing. Any

initiative taken towards this goal will facilitate the wide scale use of these alternative binders in different building components.

Acknowledgements

The authors would like to acknowledge Sembcorp Architects & Engineers Pte. Ltd. and National Research Foundation (NRF) Singapore for their funding and support in this research project.

References:

1. Wangler, T., Roussel, N., Bos, F. P., Salet, T. A., & Flatt, R. J. (2019). Digital concrete: a review. *Cement and Concrete Research*, *123*, 105780.

2. Tay, Y. W. D., Panda, B., Paul, S. C., Noor Mohamed, N. A., Tan, M. J., & Leong, K. F. (2017). 3D printing trends in building and construction industry: a review. *Virtual and Physical Prototyping*, *12*(3), 261-276.

3. Alghamdi, H., Nair, S. A., & Neithalath, N. (2019). Insights into material design, extrusion rheology, and properties of 3D-printable alkali-activated fly ash-based binders. *Materials & Design*, *167*, 107634.

4. Roussel, N. (2018). Rheological requirements for printable concretes. *Cement and Concrete Research*, *112*, 76-85.

5. Jayathilakage, R., Rajeev, P., & Sanjayan, J. (2020). Yield stress criteria to assess the buildability of 3D concrete printing. *Construction and Building Materials*, *240*, 117989.

6. Zhu, B., Pan, J., Nematollahi, B., Zhou, Z., Zhang, Y., & Sanjayan, J. (2019). Development of 3D printable engineered cementitious composites with ultra-high tensile ductility for digital construction. *Materials & Design*, *181*, 108088.

7. Markin, V., Nerella, V. N., Schröfl, C., Guseynova, G., & Mechtcherine, V. (2019). Material Design and Performance Evaluation of Foam Concrete for Digital Fabrication. *Materials*, *12*(15), 2433.

8. Rahul, A. V., Santhanam, M., Meena, H., & Ghani, Z. (2019). 3D printable concrete: Mixture design and test methods. *Cement and Concrete Composites*, *97*, 13-23.

9. Wangler, T., Lloret, E., Reiter, L., Hack, N., Gramazio, F., Kohler, M., Bernhard, M., Dillenburger, B., Buchli, J., Roussel, N. and Flatt, R., 2016. Digital concrete: opportunities and challenges. *RILEM Technical Letters*, 1, pp.67-75.

10. Paul, S. C., Tay, Y. W. D., Panda, B., & Tan, M. J. (2018). Fresh and hardened properties of 3D printable cementitious materials for building and construction. *Archives of Civil and Mechanical Engineering*, *18*(1), 311-319.

11. Panda, B., & Tan, M. J. (2018). Experimental study on mix proportion and fresh properties of fly ash based geopolymer for 3D concrete printing. *Ceramics International*, *44*(9), 10258-10265.

12. Ketel, S., Falzone, G., Wang, B., Washburn, N., & Sant, G. (2019). A printability index for linking slurry rheology to the geometrical attributes of 3D-printed components. *Cement and Concrete Composites*, *101*, 32-43.

13. Long, W. J., Tao, J. L., Lin, C., Gu, Y. C., Mei, L., Duan, H. B., & Xing, F. (2019). Rheology and buildability of sustainable cement-based composites containing micro-crystalline cellulose for 3D-printing. *Journal of Cleaner Production*, *239*, 118054.

14. Ma, G., & Wang, L. (2018). A critical review of preparation design and workability measurement of concrete material for largescale 3D printing. *Frontiers of Structural and Civil Engineering*, *12*(3), 382-400.

15. Chen, Y., Chaves Figueiredo, S., Yalçinkaya, Ç., Çopuroğlu, O., Veer, F., & Schlangen, E. (2019). The effect of viscosity-modifying admixture on the extrudability of limestone and calcined clay-based cementitious material for extrusion-based 3d concrete printing. *Materials*, *12*(9), 1374.

16. C. Sonat, C. Unluer, Investigation of the performance and thermal decomposition of MgO and MgO-SiO2 formulations, *Thermochimica Acta*, 655 (2017) 251-261.

17. C. Sonat, W.W. Teo, C. Unluer, Performance and microstructure of MgO-SiO2 concrete under different environments, *Construction and Building Materials*, 184 (2018) 549-564.

18. Khalil, A., Wang, X., & Celik, K. (2020). 3D printable magnesium oxide concrete: towards sustainable modern architecture. *Additive Manufacturing*, 101145.

19. Hay, R., & Celik, K. (2020). Hydration, carbonation, strength development and corrosion resistance of reactive MgO cement-based composites. *Cement and Concrete Research*, *128*, 105941.

20. C. Sonat, C. Unluer, Development of magnesium-silicate-hydrate (M-S-H) cement with rice husk ash, *Journal of Cleaner Production*, 211 (2019) 787-803.

21. F. Jin, K. Gu, A. Abdollahzadeh, A. Al-Tabbaa, Effects of different reactive MgOs on the hydration of MgO-activated GGBS paste, *Journal of Materials in Civil Engineering*, 27 (2013) B4014001.

22. M. Tonelli, F. Martini, A. Milanesi, L. Calucci, M. Geppi, S. Borsacchi, F. Ridi, Effect of phosphate additives on the hydration process of magnesium silicate cements, *Journal of Thermal Analysis and Calorimetry*, 138 (2019) 3311-3321.

471 23. Y. Jia, B. Wang, Z. Wu, J. Han, T. Zhang, L.J. Vandeperre, C.R. Cheeseman, Role of sodium
472 hexametaphosphate in MgO/SiO 2 cement pastes, *Cement and Concrete Research*, 89 (2016) 63-
473 71.
474 24. H. Tran, A. Scott, R. Dhakal, Mechanical and durability properties of magnesium silicate
475 hydrate binder concrete, *Magazine of Concrete Research*, (2019) 1-10.
476 25. E. Bernard, B. Lothenbach, C. Chlique, M. Wyrzykowski, A. Dauzeres, I. Pochard, C. Cau-
477 Dit-Coumes, Characterization of magnesium silicate hydrate (MSH), *Cement and concrete*
478 *research*, 116 (2019) 309-330.
479 26. D. Nied, K. Enemark-Rasmussen, E. L'Hopital, J. Skibsted, B. Lothenbach, Properties of
480 magnesium silicate hydrates (MSH), *Cement and Concrete Research*, 79 (2016) 323-332.
481 27. T. Zhang, L.J. Vandeperre, C.R. Cheeseman, Formation of magnesium silicate hydrate (MSH)
482 cement pastes using sodium hexametaphosphate, Cement and Concrete Research, 65 (2014) 8-14.
483 28. T. Zhang, E. Dieckmann, S. Song, J. Xie, Z. Yu, C. Cheeseman, Properties of magnesium
484 silicate hydrate (MSH) cement mortars containing chicken feather fibres, *Construction and*
485 *Building Materials*, 180 (2018) 692-697.
486 29. G. Mármol, H. Savastano Jr, Study of the degradation of non-conventional MgO-SiO2 cement
487 reinforced with lignocellulosic fibers, *Cement and Concrete Composites*, 80 (2017) 258-267.
488 30. T. Zhang, C. Cheeseman, L. Vandeperre, Development of low pH cement systems forming
489 magnesium silicate hydrate (MSH), *Cement and Concrete Research*, 41 (2011) 439-442.
490 31. T. Zhang, L.J. Vandeperre, C.R. Cheeseman, Magnesium-silicate-hydrate cements for
491 encapsulating problematic aluminium containing wastes, *Journal of Sustainable Cement-Based*
492 *Materials*, 1 (2012) 34-45.
493 32. Tay, Y. W. D., Qian, Y., & Tan, M. J. (2019). Printability region for 3D concrete printing
494 using slump and slump flow test. *Composites Part B: Engineering*, 174, 106968.
495 33. Laskar, A. I. (2009). Correlating slump, slump flow, vebe and flow tests to rheological
496 parameters of high-performance concrete. *Materials Research*, *12*(1), 75-81.
497 34. De Schutter, G., & Feys, D. (2016). Pumping of fresh concrete: insights and
498 challenges. *RILEM Technical Letters*, *1*, 76-80.
499 35. Panda, B., Ruan, S., Unluer, C., & Tan, M. J. (2019). Improving the 3D printability of high
500 volume fly ash mixtures via the use of nano attapulgite clay. *Composites Part B: Engineering*, *165*,
501 75-83.

36. Panda, B., Paul, S. C., Mohamed, N. A. N., Tay, Y. W. D., & Tan, M. J. (2018). Measurement of tensile bond strength of 3D printed geopolymer mortar. *Measurement*, *113*, 108-116.

37. Panda, B., Lim, J. H., & Tan, M. J. (2019). Mechanical properties and deformation behaviour of early age concrete in the context of digital construction. *Composites Part B: Engineering*, *165*, 563-571.

38. ASTM C109/C109M-13, Standard Test Method for Compressive Strength of Hydraulic Cement Mortars (Using 2-in. or [50-mm] Cube Specimens), ASTM Committee C01, West Conshohocken, PA 19428-2959, United States, 2013, p. 10.

39. Panda, B., Mohamed, N., Ahamed, N., Paul, S. C., Bhagath Singh, G. V. P., Tan, M. J., & Šavija, B. (2019). The effect of material fresh properties and process parameters on buildability and interlayer adhesion of 3D printed concrete. *Materials*, *12*(13), 2149.

40. H. Tran, A. Scott, Strength and workability of magnesium silicate hydrate binder systems, *Construction and Building Materials*, 131 (2017) 526-535.

41. F. Jin, A. Al-Tabbaa, Strength and hydration products of reactive MgO–silica pastes, *Cement and Concrete Composites*, 52 (2014) 27-33.

42. Sonat, C., Dung, N. T., & Unluer, C. (2017). Performance and microstructural development of MgO–SiO2 binders under different curing conditions. *Construction and Building Materials*, *154*, 945-955.

43. Landrou, G., Brumaud, C., & Habert, G. (2018). Influence of magnesium on deflocculated kaolinite suspension: Mechanism and kinetic control. *Colloids and Surfaces A: Physicochemical and Engineering Aspects*, 544, 196-204.

44. Wolfs, R. J. M., Bos, F. P., & Salet, T. A. M. (2018). Early age mechanical behaviour of 3D printed concrete: Numerical modelling and experimental testing. *Cement and Concrete Research*, 106, 103-116.

45. Panda, B., Paul, S. C., & Tan, M. J. (2017). Anisotropic mechanical performance of 3D printed fiber reinforced sustainable construction material. *Materials Letters*, *209*, 146-149.

46. Ma, Guowei, Zhijian Li, Li Wang, Fang Wang, and Jay Sanjayan. (2019) Mechanical anisotropy of aligned fiber reinforced composite for extrusion-based 3D printing. *Construction and Building Materials*, 202, 770-783.

531 47. Z. Li, T. Zhang, J. Hu, Y. Tang, Y. Niu, J. Wei, Q. Yu, Characterization of reaction products
532 and reaction process of MgO–SiO2–H2O system at room temperature, *Constr. Build. Mater.,*
533 (2014) 252-259.
534 48. B. Lothenbach, D. Nied, E. L'Hôpital, G. Achiedo, A. Dauzères, Magnesium and calcium
535 silicate hydrates, *Cem. Concr. Res.,* 77 (2015) 60-68.
536 49. C. Sonat, N. Dung, C. Unluer, Performance and microstructural development of MgO–SiO2
537 binders under different curing conditions, *Constr. Build. Mater.,* 154 (2017) 945-955.
538 50. Y. Zhang, Y. Li, Y. Dai, Formation of magnesium silicate hydrate in the Mg (OH) 2-SiO2
539 suspensions and its influence on the properties of magnesia castables, *Ceramics International*, 44
540 (2018) 21365-21373.

List of Tables

Table 1 Chemical composition and physical properties of the binder components.

Materials	Content (%)								SSA (m^2/g)	LOI (%)
	MgO	CaO	SiO_2	Al_2O_3	C	P_2O_5	Fe_2O_3	K_2O		
MgO	>91.5	1.6	2.0	<0.7	-	-	-	-	35.7	6.3
MS	-	-	>90.0	-	-	-	-	-	17.0	2.2

Table 2 Mix compositions used in this study.

Mix	Binder composition		Water-to-binder	SP
	MgO (%)	MS (%)	(w/b) ratio	dosage (%)
M1	50	50	0.4	1.5
M2			0.5	1.5
M3			0.4	2.5
M4			0.5	2.5
M5	70	30	0.4	1.5
M6			0.5	1.5
M7			0.4	2.5
M8			0.5	2.5

Table 3 Shape retention factors (SRF) of 3D printed MgO-SiO_2 binders.

Mix	SRF
M3	~1.0
M5	~1.84
M7	~2.32

Table 4 28-day compressive strengths of cast MgO-SiO_2 samples

Mix	Compressive strength (MPa)	Relative error (±)
M3	44.3	0.6
M5	38.3	1.0
M7	36.2	0.9

Table 5 Elemental composition (wt.%) of mix M3 after 28 days of curing

C	O	Mg	Si
5.77 ± 1.11	51.82 ± 2.41	21.26 ± 2.92	21.15 ± 4.66

List of Figures

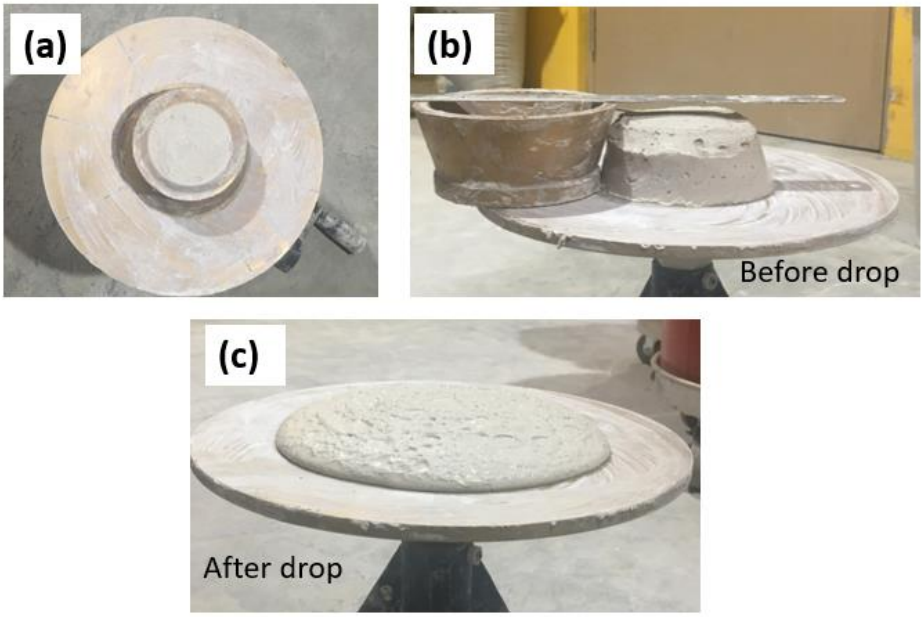

Fig. 1 Photos showing the (a) slump and flow table test setup; and behaviour of the MgO-SiO_2 pastes (b) before and (c) after drop

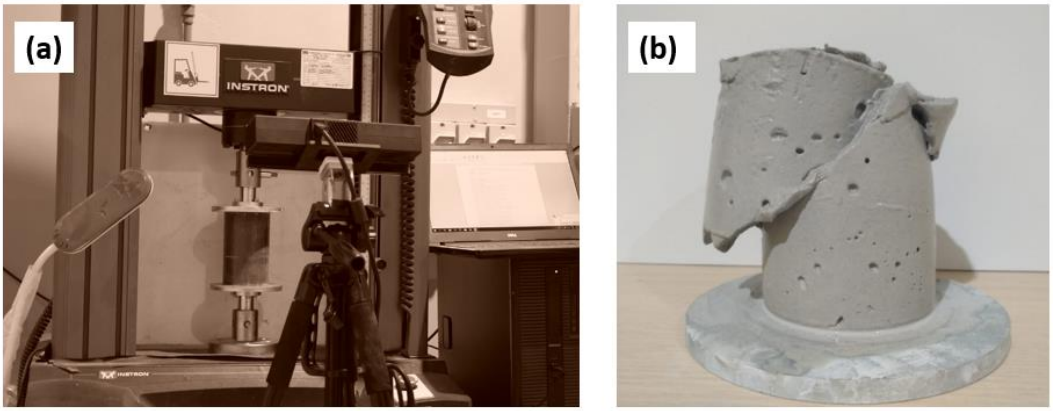

Fig. 2 Photos showing the (a) experimental setup and (b) typical shear failure of the MgO-SiO_2 pastes during uniaxial compression test

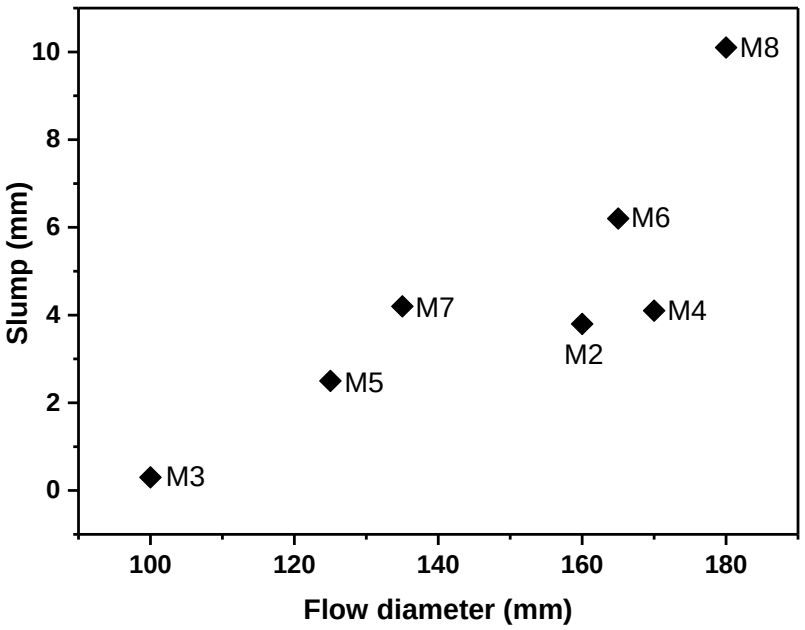

Fig. 3 Slump values and flow diameters of MgO-SiO_2 pastes

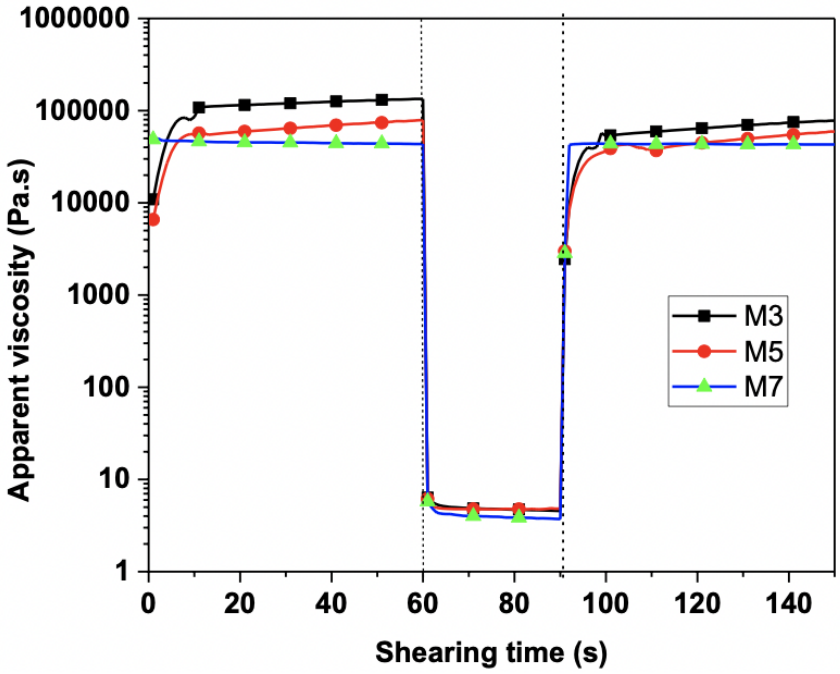

Fig. 4 Viscosity recovery of MgO-SiO_2 pastes

Fig. 5 3D printed section via the use of mix M3

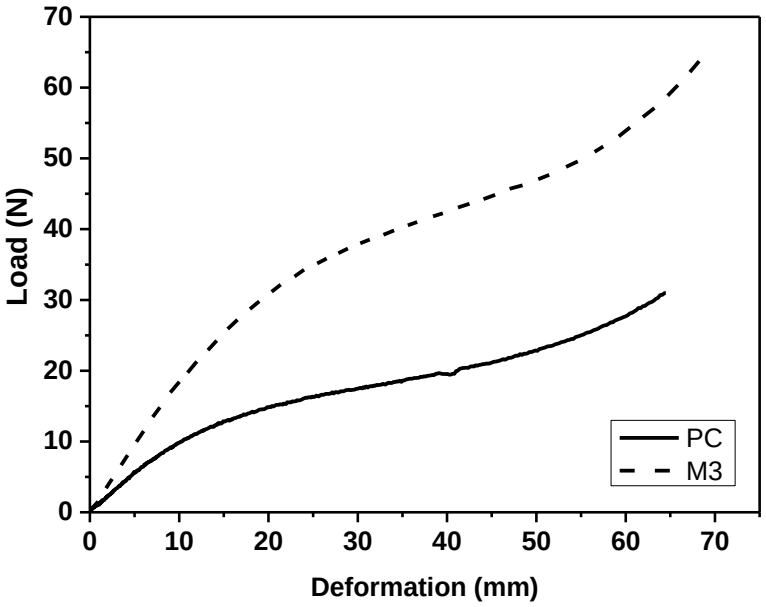

Fig. 6 Load-deformation curves of M3 ($MgO\text{-}SiO_2$) and PC mixes after 15 minutes of initial contact with water

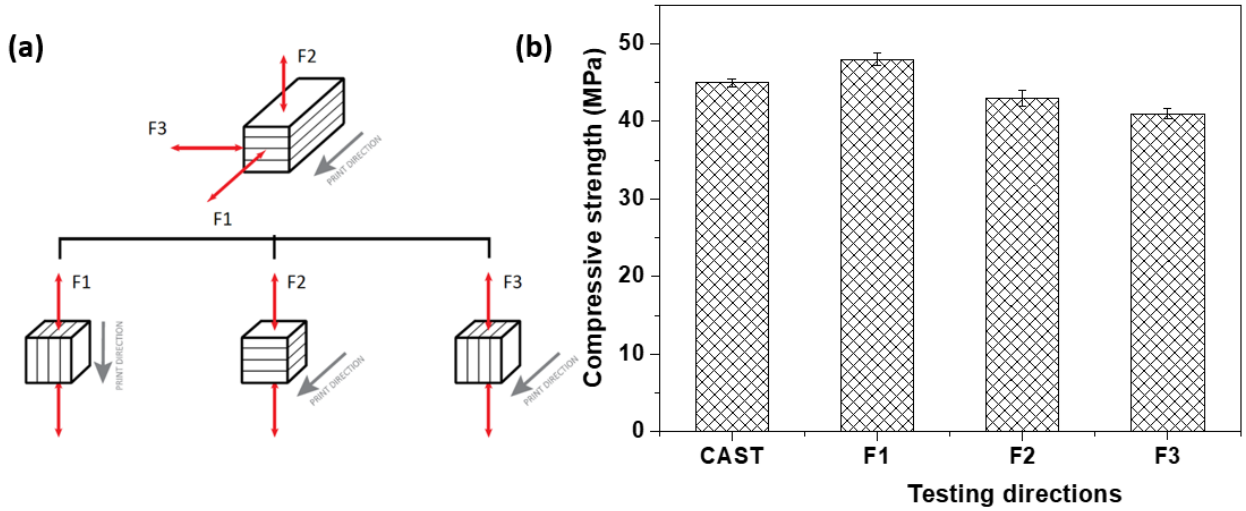

Fig. 7 Illustration of (a) the directional compressive testing orientations with respect to print direction, and (b) mechanical properties of cast and 3D printed mix M3 in 3 directions

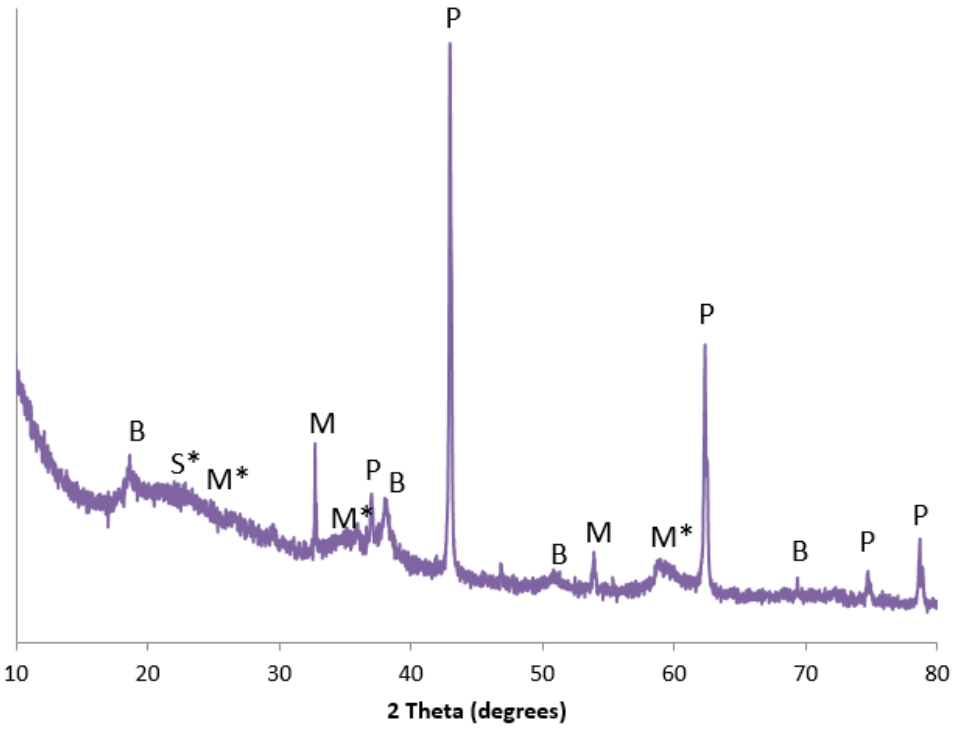

Fig. 8 XRD pattern of mix M3 at 28 days

(B: Brucite, P: Periclase, M: Magnesite, M*: M-S-H, S*: SiO_2)

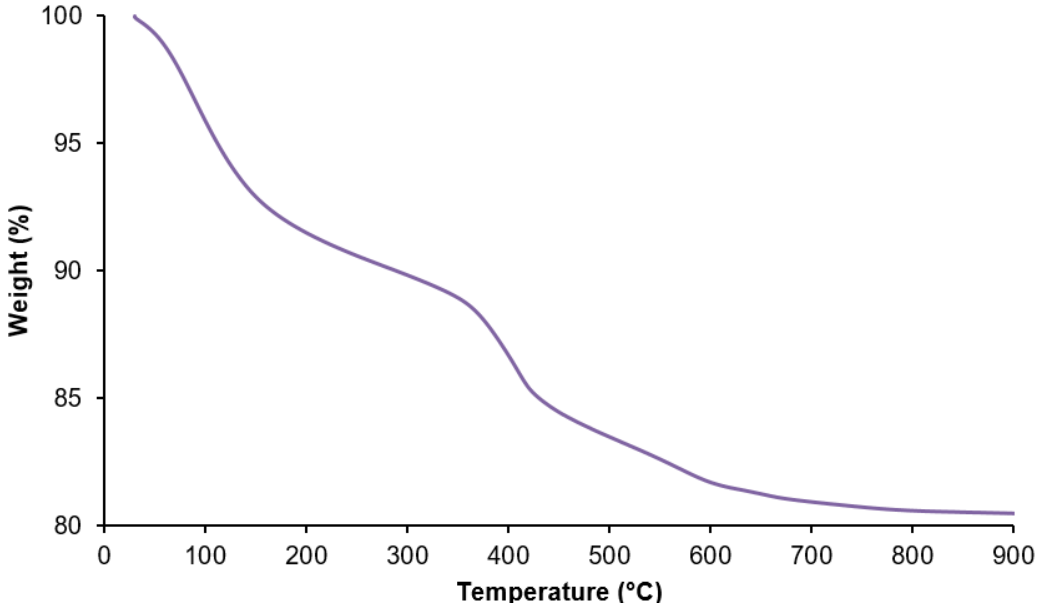

(a)

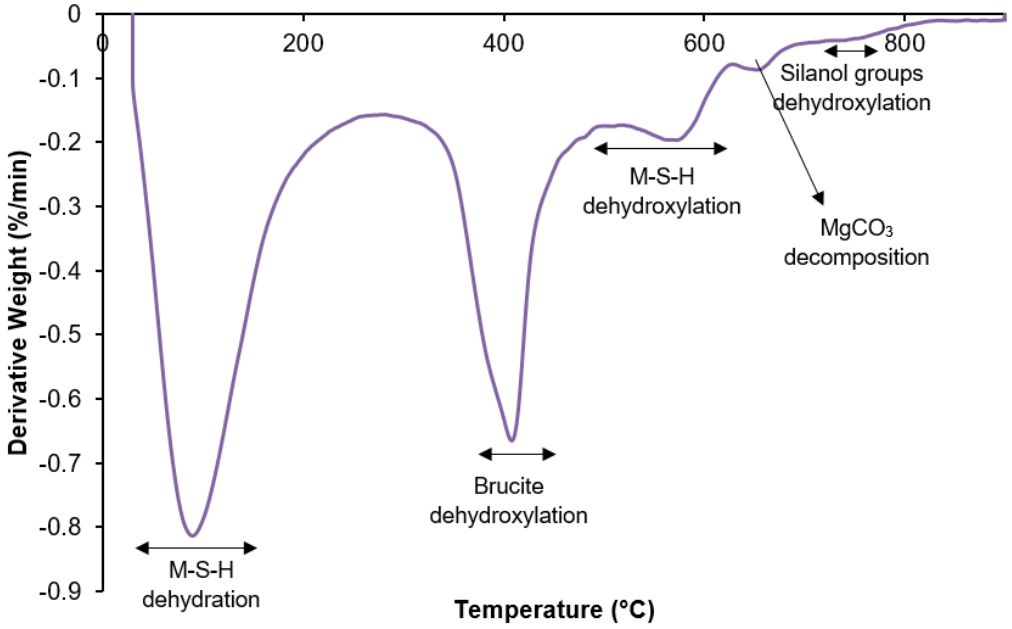

(b)

Fig. 9 Thermogravimetric analysis results showing (a) TGA and (b) DTG plots of mix M3 at 28 days

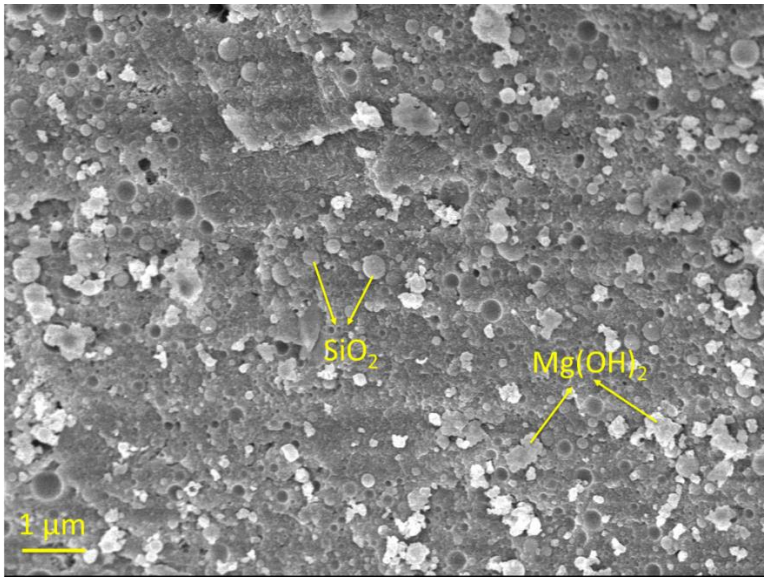

Fig. 10 FESEM image of mix M3 at 28 days

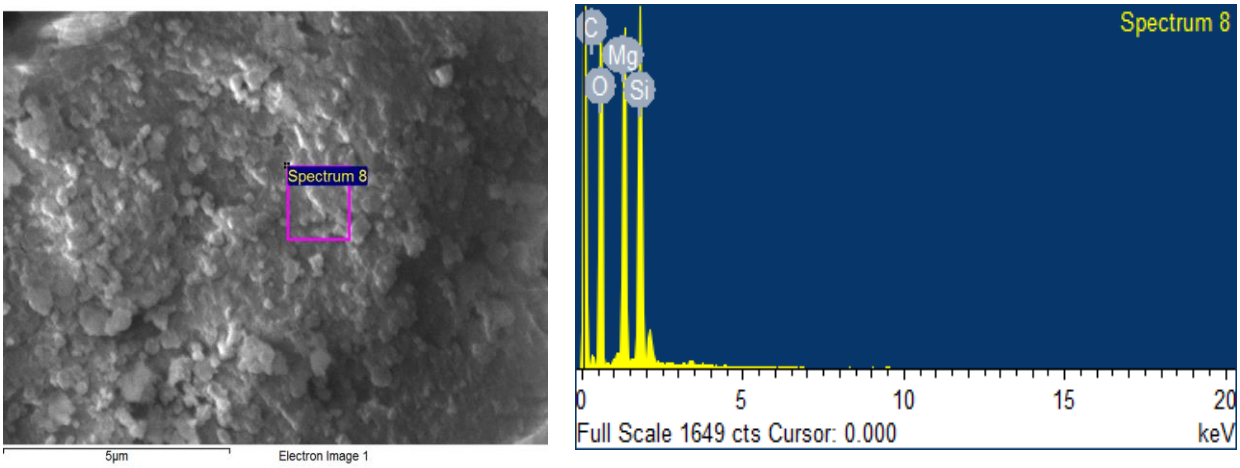

(a) (b)

Fig. 11 Images taken during the EDS analysis of mix M3 at 28 days, showing: (a) region of the specimen, where multiple EDS analyses have been performed and (b) representative EDS elemental analysis of the spectrum indicated in Fig. 11(a)